Inorganic Chemistry

Article

pubs.acs.org/IC

# Photophysical Properties of β-Substituted Free-Base Corroles

Christopher M. Lemon, Robert L. Halbach, Michael Huynh, and Daniel G. Nocera*

Department of Chemistry and Chemical Biology, Harvard University, 12 Oxford Street, Cambridge, Massachusetts 02138, United States

Supporting Information

**ABSTRACT:** Corroles are an emergent class of fluorophores that are finding an application and reaction chemistry to rival their porphyrin analogues. Despite a growing interest in the synthesis, reactivity, and functionalization of these macrocycles, their excited-state chemistry remains undeveloped. A systematic study of the photophysical properties of β-substituted corroles was performed on a series of free-base β-brominated derivatives as well as a β-linked corrole dimer. The singlet and triplet electronic states of these compounds were examined with steady-state and time-resolved spectroscopic methods, which are complemented with density functional theory (DFT) and time-dependent DFT calculations to gain insight into the nature of the electronic structure. Selective bromination of a single molecular edge manifests in a splitting of the Soret band into *x* and *y* polarizations, which is a consequence of asymmetry of the molecular axes. A pronounced heavy atom effect is the primary determinant of the photophysical properties of these free-base corroles; bromination decreases the fluorescence quantum yield (from 15% to 0.47%) and lifetime (from 4 ns to 80 ps) by promoting enhanced intersystem crossing, as evidenced by a dramatic increase in $k_{nr}$ with bromine substitution. The nonbrominated dimer exhibits absorption and emission features comparable to those of the tetrabrominated derivative, suggesting that oligomerization provides a means of red-shifting the spectral properties akin to bromination but without decreasing the fluorescence quantum yield.

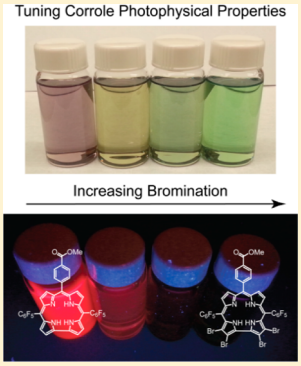


## INTRODUCTION

Porphyrins possess unique electronic and photophysical properties that engender their use as imaging agents,[1−4] photosensitizers for photodynamic therapy,[5−7] light-harvesting antennas,[8−11] and optical sensors.[12−15] A related class of molecules is corroles, which, like porphyrins, are 18 π-electron tetrapyrrole macrocycles but with a contracted 23-atom core versus the 24-atom core of porphyrins. This contracted core arises from a direct pyrrole−pyrrole linkage to yield three meso carbons bridging pyrrole units, unlike the four meso carbons of a porphyrin. Corroles have been historically difficult to synthesize with the first preparations involving the cyclization of the linear precursor biladiene-*ac*.[16,17] With the advent of facile one-pot methods,[18−21] corrole chemistry has expanded with emphasis on both the synthesis and peripheral functionalization of the macrocycle.[22−27] The availability of corroles as a result of these synthetic methods has led to many applications,[28−30] including their function as molecular catalysts,[31−36] photosensitizers,[37−39] singlet oxygen photogenerators,[40,41] and imaging agents.[42] Despite these advances, there have been comparatively few photophysical studies of free-base corroles. Some of these studies include the elucidation of photophysics as a function of meso-substitution,[40,41,43−46] N−H tautomerization,[47−50] and higher order architectures such as corrole−fluorophore dyads.[51−53]

A desirable property of any fluorophore is the ability to tune its absorbance and emission wavelengths, as well as the excited-state lifetime. Modulation of spectral features to achieve a desired optical window is important for any imaging or sensing application, especially for those that function in the biological milieu. Free-base corroles have appreciable fluorescence quantum yields and excited-state lifetimes of several nanoseconds.[40,43] The effect of substitution at the meso positions of the corrole appears to have a more pronounced influence on photophysical properties than it does for porphyrins. Spurred by these observations, we were interested in delineating the effect of β-substitution on the electronic structure and excited-state properties of corroles. We find that the electronic spectral properties are governed by the (*x*,*y*) asymmetry of the corrole ring. As observed by Gross and co-workers for Al and Ga corroles,[54] β-substitution with halogen causes a severe perturbation to the photophysics of the corrole, arising from a pronounced heavy atom effect. Corrole dimerization at the β-position provides a means of red-shifting the spectral properties akin to bromination but without decreasing the fluorescence quantum yield. Such design principles are useful for the implementation of corroles for sensing applications.

## EXPERIMENTAL SECTION

**Materials.** The following materials were used as received: hexanes, acetone, ethanol (EtOH), methanol (MeOH), chloroform ($CHCl_3$), dichloromethane ($CH_2Cl_2$), pentane, inhibitor-free tetrahydrofuran (THF), acetonitrile (MeCN), toluene, benzonitrile (PhCN), dimethyl sulfoxide (DMSO), pyrrole, indium(III) chloride ($InCl_3$), sodium hydroxide (NaOH) beads, methyl 4-formylbenzoate, 2,3-dichloro-5,6-dicyano-1,4-benzoquinone (DDQ), *N*-bromosuccinimide (NBS), and pentafluorobenzaldehyde from Sigma-Aldrich; sodium bicarbonate ($NaHCO_3$), sodium sulfate ($Na_2SO_4$), and sodium chloride (NaCl)

**Received:** December 4, 2014
**Published:** February 25, 2015





DOI: 10.1021/ic502860g
*Inorg. Chem.* 2015, 54, 2713−2725

from Mallinckrodt; hydrochloric acid (HCl) from EMD; silica gel 60 Å 230−400 mesh ASTM from Whatman; and chloroform-*d* ($CDCl_3$) from Cambridge Isotope Laboratories. Argon gas (Airgas) was passed over a Drierite column prior to use. The compounds 5-pentafluorophenyldipyrromethane (**1**)[55,56] and 5,10,15,20-tetraphenylporphyrin ($H_2TPP$)[57] were prepared according to literature procedures or slight modifications thereof.

**Corrole Synthesis.** In a 1 L round-bottom flask, 1.58 g of 5-pentafluorophenyldipyrromethane (**1**) (5.06 mmol) and 0.41 g of methyl 4-formylbenzoate (2.5 mmol) were dissolved in 250 mL of MeOH. A solution of HCl was prepared by dissolving 12.5 mL of concentrated HCl (12 M) in 250 mL of $H_2O$. The acid solution was added to the MeOH solution and stirred at room temperature for 1 h. Over the course of the reaction, the solution became cloudy, and a red-brown color developed. The reaction mixture was poured into a 2 L separatory funnel, and the product was extracted with $CHCl_3$ (200 mL ×3). The combined organics were washed with water (×2), dried over $Na_2SO_4$, and the solution was diluted to a volume of 1 L with $CHCl_3$; 1.71 g of DDQ (2.51 mmol) was added, and this solution immediately turned dark. The reaction mixture was stirred overnight at room temperature. The crude reaction mixture was concentrated to a volume of ∼200 mL and then poured onto a silica gel column packed with hexanes. All fluorescent material was collected using $CHCl_3$ as the eluent. The product was purified on a silica gel column packed with hexanes, using hexanes then 1:1 hexanes/$CH_2Cl_2$ to elute **2** as a purple solution. A second macrocyclic product (**3**) was identified at the top of the column and was isolated using 100% $CH_2Cl_2$ as the eluent to afford a green solution. After solvent removal, 0.33 g (17% yield) of **3** was isolated as a shiny purple solid. Compound **2**, which was initially obtained as a black solid, was further purified on a silica gel column packed with hexanes, using hexanes then 1:1 hexanes/$CH_2Cl_2$ as the eluent. After solvent removal, 0.98 g (51% yield) of **2** was obtained as a purple solid.

*10-(4-Methoxycarbonylphenyl)-5,15-bis(pentafluorophenyl)-corrole (**2**).* $^1$H NMR (500 MHz, $CDCl_3$) $\delta$ 4.10 (s, 3H), 8.27 (d, $J$ = 8.1 Hz, 2H), 8.45 (d, $J$ = 8.1 Hz, 2H), 8.59 (bs, 2H), 8.66 (d, $J$ = 4.8 Hz, 2H), 8.73 (d, $J$ = 4.6 Hz, 2H), 9.14 (d, $J$ = 4.3 Hz, 2H). $^{19}$F NMR (376 MHz, $CH_2Cl_2$) $\delta$ −163.98 (m, 4F), −155.15 (m, 2F), −140.15 (dd, $J^1$ = 28.9 Hz, $J^2$ = 6.5 Hz, 4F). Anal. Calcd for $(M + H)^+$, M = $C_{39}H_{18}F_{10}N_4O_2$: 765.1270; Found ESI-MS: 765.1252. UV−vis (toluene), $\lambda$ in nm ($\varepsilon$ in $10^3$ $M^{-1}$ $cm^{-1}$): 424 (99), 525 (7.3), 565 (16), 615 (9.3), 640 (5.8).

*3-[10′-(4-Methoxycarbonylphenyl)-5′,15′-bis-(pentafluorophenyl)corrole-3′-yl]-10-(4-methoxycarbonylphenyl)-5,15-bis(pentafluorophenyl)corrole (**3**).* $^1$H NMR (500 MHz, $CDCl_3$) $\delta$ 4.07 (s, 6H), 8.21 (d, $J$ = 7.7 Hz, 4H), 8.25 (d, $J$ = 8.0 Hz, 2H), 8.41 (d, $J$ = 8.2 Hz, 4H), 8.47 (d, $J$ = 4.8 Hz, 2H), 8.60 (d, $J$ = 4.7 Hz, 2H), 8.71 (d, $J$ = 4.7 Hz, 2H), 8.74 (d, $J$ = 4.3 Hz, 2H), 9.16 (s, 2H), 9.17 (d, $J$ = 4.2 Hz, 2H). $^{19}$F NMR (376 MHz, $CH_2Cl_2$) $\delta$ −167.62 (bs, 2F), −165.29 (m, 2F), −163.97 (m, 4F), −157.03 (bs, 2F), −155.10 (m, 2F), −141.33 (bs, 2F), −139.98 (dd, $J^1$ = 25.9 Hz, $J^2$ = 6.5 Hz, 4F),−139.49 (bs, 2F). Anal. Calcd for $(M + H)^+$, M = $C_{78}H_{34}F_{20}N_8O_4$: 1527.2384; Found ESI-MS: 1527.2322. UV−vis (toluene), $\lambda$ in nm ($\varepsilon$ in $10^3$ $M^{-1}$ $cm^{-1}$): 418 (144), 448 (91), 547 (20), 582 (34), 627 (27), 656 (34).

**Preparation of Bromocorroles.** In a 100 mL round-bottom flask, 82 mg (0.11 mmol) of **2** was dissolved in 20 mL of $CH_2Cl_2$. A solution of *N*-bromosuccinimide (NBS) was prepared by dissolving 52 mg (0.29 mmol) of the compound in 10 mL of MeCN. The NBS solution was slowly added to the corrole solution, ∼1 mL at a time, using a pipet over the course of ∼5 min. The resultant blue-green solution was stirred at room temperature for 1 h. The crude reaction mixture was extracted with $CHCl_3$, washed with water, saturated $NaHCO_3$, and brine, then dried over $Na_2SO_4$ and brought to dryness. The residue was purified on a silica gel column packed with hexanes using 1:1 hexanes/$CHCl_3$ as the eluent. Fractions were collected in 100 mL aliquots. Fractions 1−3 were blue-green in color and were identified as compound **5** by $^1$H NMR, affording 27 mg (25% yield) of the product. Fractions 5−9 were violet in color and were identified as compound **4** by $^1$H NMR, affording 35 mg (35% yield) of the product. Later-eluting fractions were identified as monobrominated corroles (2-bromo-**2** and 3-bromo-**2**), as well as putative decomposition products on the basis of $^1$H NMR.

*2,3-Dibromo-10-(4-methoxycarbonylphenyl)-5,15-bis-(pentafluorophenyl)corrole (**4**).* $^1$H NMR (500 MHz, $CDCl_3$) $\delta$ 4.08 (s, 3H), 8.26 (d, $J$ = 8.1 Hz, 2H), 8.44 (d, $J$ = 8.1 Hz, 2H), 8.57 (d, $J$ = 4.4 Hz, 1H), 8.62 (d, $J$ = 4.8 Hz, 1H), 8.66 (overlapping d, $J$ = 5.0 Hz, 1H), 8.67 (overlapping d, $J$ = 4.8 Hz, 1H), 8.81 (d, $J$ = 4.7 Hz, 1H), 9.39 (d, $J$ = 4.4 Hz, 1H). $^{19}$F NMR (376 MHz, $CH_2Cl_2$) $\delta$ −164.64 (m, 2F), −163.42 (m, 2F), −155.02 (m, 1F), −154.07 (m, 1F), −140.31 (d, J = 27.2 Hz, 2F), −140.11 (d, $J$ = 27.1 Hz, 2F). Anal. Calcd for $(M + H)^+$, M = $C_{39}H_{16}Br_2F_{10}N_4O_2$: 922.9460; Found ESI-MS: 922.9462. UV−vis (toluene), $\lambda$ in nm ($\varepsilon$ in $10^3$ $M^{-1}$ $cm^{-1}$): 427 (93), 528 (7.5), 565 (15), 597 (8.9), 648 (14).

*2,3,17-Tribromo-10-(4-methoxycarbonylphenyl)-5,15-bis-(pentafluorophenyl)corrole (**5**).* $^1$H NMR (500 MHz, $CDCl_3$) $\delta$ 4.09 (s, 3H), 8.24 (d, $J$ = 8.1 Hz, 2H), 8.45 (d, $J$ = 8.0 Hz, 2H), 8.58 (d, $J$ = 4.8 Hz, 1H), 8.63 (d, $J$ = 4.6 Hz, 2H), 8.73 (d, $J$ = 4.7 Hz, 1H), 9.34 (s, 1H). $^{19}$F NMR (376 MHz, $CH_2Cl_2$) $\delta$ −164.38 (m, 2F), −164.09 (m, 2F), −154.60 (m, 1F), −154.01 (m, 1F), −140.92 (d, $J$ = 27.0 Hz, 2F), −140.14 (d, $J$ = 27.3 Hz, 2F). Anal. Calcd for $(M + H)^+$, M = $C_{39}H_{15}Br_3F_{10}N_4O_2$: 1000.8565; Found ESI-MS: 1000.8555. UV−vis (toluene), $\lambda$ in nm ($\varepsilon$ in $10^3$ $M^{-1}$ $cm^{-1}$): 423 (100), 437 (92), 531 (7.3), 570 (16), 598 (11), 650 (19).

*2,3,17,18-Tetrabromo-10-(4-methoxycarbonylphenyl)-5,15-bis-(pentafluorophenyl)corrole (**6**).* In a 100 mL round-bottom flask, 80 mg (0.10 mmol) of **2** was dissolved in 15 mL of MeCN. A solution of NBS was prepared by dissolving 87 mg (0.49 mmol) of the compound in 15 mL of $CH_2Cl_2$. The NBS solution was slowly added to the corrole solution, ∼1 mL at a time using a pipet over the course of ∼5 min. The resultant blue-green solution was stirred at room temperature for 1 h. The crude reaction mixture was washed with water, saturated $NaHCO_3$, and brine, then dried over $Na_2SO_4$, and brought to dryness. The residue was purified on a silica gel column packed with hexanes using hexanes then 1:1 hexanes/$CH_2Cl_2$ as the eluent. The product eluted as a blue-green solution. The solvent was removed to afford 67 mg (62% yield) of the title compound as a purple solid. $^1$H NMR (500 MHz, $CDCl_3$) $\delta$ 4.08 (s, 3H), 8.20 (d, $J$ = 8.0 Hz, 2H), 8.43 (d, $J$ = 8.1 Hz, 2H), 8.51 (d, $J$ = 4.7 Hz, 2H), 8.59 (d, $J$ = 4.6 Hz, 2H). $^{19}$F NMR (376 MHz, $CH_2Cl_2$) $\delta$ −164.04 (m, 4F), −154.03 (m, 2F), −140.46 (dd, $J^1$ = 27.9 Hz, $J^2$ = 6.2 Hz, 4F). Anal. Calcd for $(M + H)^+$, M = $C_{39}H_{14}Br_4F_{10}N_4O_2$: 1080.7650; Found ESI-MS: 1080.7699. UV−vis (toluene), $\lambda$ in nm ($\varepsilon$ in $10^3$ $M^{-1}$ $cm^{-1}$): 423 (98), 440 (88), 538 (8.1), 575 (19), 607 (13), 655 (19).

**Physical Measurements.** $^1$H NMR spectra were recorded at 23 °C on a Varian Inova-500 NMR spectrometer at the Harvard University Department of Chemistry and Chemical Biology Laukien-Purcell Instrumentation Center. All spectra were internally referenced to the residual solvent signal ($\delta$ = 7.26 for $CHCl_3$ in $CDCl_3$).[58] $^{19}$F NMR spectra were recorded at 25 °C on a Varian Mercury-400 NMR spectrometer and externally referenced to $\alpha,\alpha,\alpha$-trifluorotoluene ($\delta$ = −63.72). Mass spectra were recorded on a Bruker micrO-TOF-QII LCMS ESI-TOF mass spectrometer in positive ion mode. All spectra were externally calibrated with sodium formate. UV−vis absorption spectra were acquired using a Cary 5000 spectrometer (Agilent). Steady-state emission spectra were recorded on a Photon Technology International (PTI) QM 4 fluorometer equipped with a 150 W Xe arc lamp and a Hamamatsu R2658 photomultiplier tube. Relative quantum yields of corroles in toluene were calculated using $H_2TPP$ in toluene as the reference according to the following equation

$$\Phi_{sam} = \Phi_{ref}\left(\frac{\nabla_{sam}}{\nabla_{ref}}\right)\left(\frac{\eta_{sam}}{\eta_{ref}}\right)^2 \quad (1)$$

where $\nabla$ is the slope of the plot of integrated fluorescence intensity versus absorbance (constructed using 5 points), $\eta$ is the refractive index of the solvent (taken to be 1.4961 for toluene),[59] and $\Phi_{ref}$ is the emission quantum yield of the reference. $\Phi_{ref}$ was taken to be 0.11 for an aerated sample of $H_2TPP$ in toluene.[60] Corrole samples for lifetime ($\tau_0$) measurements and transient absorbance spectra were prepared


DOI: 10.1021/ic502860g
Inorg. Chem. 2015, 54, 2713−2725

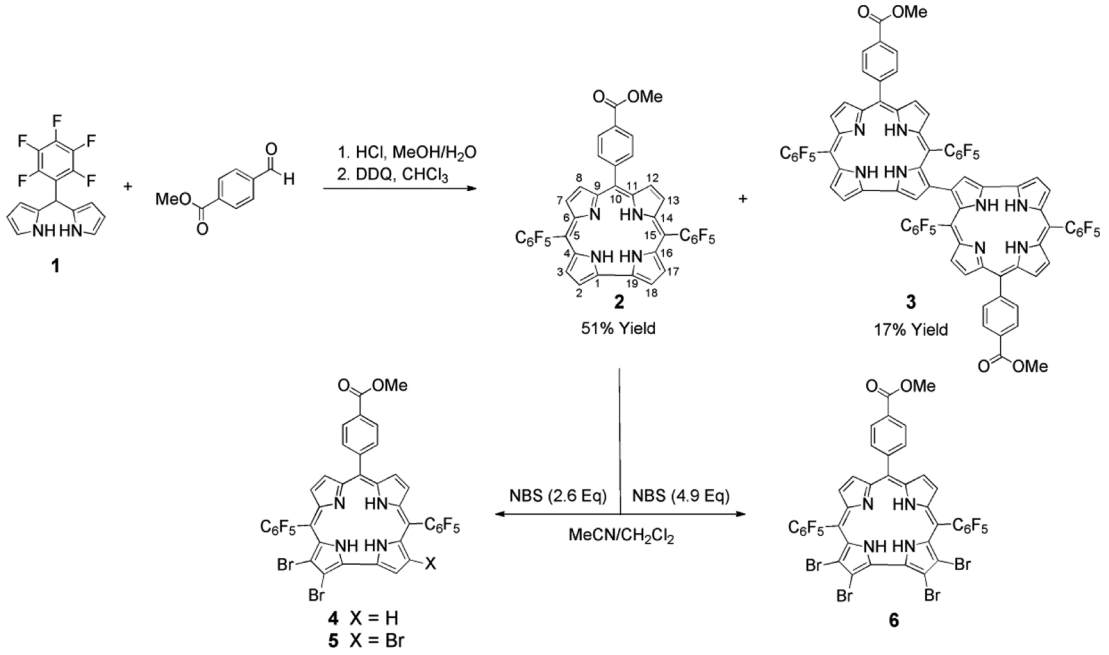


**Figure 1.** Synthesis of free-base corrole **2** and subsequent bromination with NBS to afford a series of $\beta$-brominated corroles **4**–**6**.

using three freeze–pump–thaw (fpt) cycles at vacuum pressures below $10^{-4}$ Torr.

Femtosecond emission lifetime measurements were acquired using a Libra-F-HE (Coherent) chirped–pulse amplified Ti:sapphire laser system.[61] The 800 nm laser output was used to pump an OperA Solo (Coherent) optical parametric amplifier (OPA); excitation pulses of 400 nm were produced via fourth harmonic generation of the signal using a BBO crystal, and the pulse power was attenuated to 2–6 mW at the sample using neutral density filters. Emission lifetimes were measured on a Hamamatsu C4334 Streak Scope streak camera, which has been described elsewhere.[62] The emission signal was collected over a 140 nm window centered at 680 or 700 nm with 50, 20, 2, or 1 ns time windows using a Stanford Research Systems DG535 delay generator.

Nanosecond transient absorption (TA) spectra of corroles were acquired using a previously reported system.[63,64] Pump light was provided by the third harmonic (355 nm) of a Quanta-Ray Nd:YAG laser (Spectra Physics) operating at 10 Hz. The pump light was passed through a BBO crystal in an optical parametric oscillator (OPO), yielding a visible frequency that was tuned to 430 nm to excite the sample. Excitation light was attenuated to 100–300 $\mu$J per pulse for all experiments using neutral density filters. Probe white light was generated using a 75 W Xe-arc lamp (PTI). The probe beam was aligned with the sample, while the laser pump beam was positioned at 15° with respect to the white light probe, and both beams were focused on the sample. After exiting the sample, the light entered either a Triax 320 (Jobin Yvon Horiba) or a iHR320 monochromator (Horiba Scientific) and was dispersed by a blazed grating (500 nm, 300 grooves/mm) centered at 500 nm. The entrance and exit slits of the monochromator were set to provide a spectral resolution of 4 nm. TA spectra were collected using a gated intensified CCD camera (DH520–25F-01, Andor Technology). Acquisition delays and gate times for the CCD were set using a Stanford Research Systems DG535 delay generator, which was synchronized to the Q-switch output of the laser. The final data were calculated from a combination of four spectra: $I$ (pump on/probe on), $I_F$ (pump on/probe off), $I_0$ (pump off/probe on), and $I_B$ (pump off/probe off). The resultant TA spectra were obtained using the following equation:

$$\Delta OD = -\log\left(\frac{I - I_F}{I_0 - I_B}\right) \quad (2)$$

thereby correcting for both sample emission and extraneous background light. To acquire these four spectra, pump and probe beams were selectively exposed to the sample using electronically controlled shutters (Uniblitz T132, Vincent Associates), which were triggered using a Stanford Research Systems DG535 delay generator synchronized to the Q-switch output of the laser. For TA single wavelength kinetics, output signal from the sample was passed through a 450 nm long pass filter and then amplified by a photomultiplier tube (R928, Hamamatsu) and collected on a 1 GHz digital oscilloscope (9384CM, LeCroy); acquisition was triggered using a photodiode to collect scattered laser excitation light.

**Computational Details.** Density functional theory (DFT) calculations were performed with the hybrid functional Becke-3 parameter exchange functional[65−67] and the Lee–Yang–Parr nonlocal correlation functional (B3LYP)[68] as implemented in the Gaussian 09, Revision D.01 software package.[69] For light atoms (H, C, N, O, and F), a polarized split-valence triple-$\zeta$ basis set that includes p functions on hydrogen atoms and d functions on other atoms (i.e., 6-311G(d,p) or 6-311G** basis set) was used. The LANL2DZ basis set was used for bromine atoms with the inclusion of an effective core potential (ECP).[70,71] All calculations were performed with a polarizable continuum (PCM) solvation model in toluene using a polarizable conductor calculation model (CPCM).[72,73] All geometries were confirmed as local minima structures by calculating the Hessian matrix and ensuring that no imaginary eigenvalues were present. Excited-state calculations were performed using time-dependent DFT (TD-DFT)[74−78] with the same functionals, basis sets, and solvation details as the ground state, but with the inclusion of diffuse functions on all light atoms (i.e., 6-311++G** basis set). Excited-state energies were computed for the 10 or 15 lowest singlet and triplet excited states. All optimized geometries and molecular orbitals were rendered in the program Avogadro.[79] Simulated UV–vis spectra were generated in the program Gauss View 5 by broadening transition lines with Gaussian functions with a half width of 0.08 eV.

**X-ray Crystallographic Details.** Diffraction-quality crystals of **2** were obtained by slow evaporation of a 1:1 mixture of pentane and THF under $N_2$ at 20 °C, affording crystals as purple blocks; a single crystal was cut from a larger one for the X-ray diffraction study. Crystals of **3** and **6** were obtained by dissolving each compound in a minimal amount of a 1:1 mixture of pentane and THF and cooling the resultant solutions to −40 °C, affording crystals as purple blocks. Low-temperature (100 K) X-ray diffraction data were collected on a Bruker


DOI: 10.1021/ic502860g
Inorg. Chem. 2015, 54, 2713–2725

three-circle platform goniometer equipped with an Apex II CCD detector and an Oxford cryostream cooling device, performing $\varphi$ and $\omega$ scans. Radiation was generated from a graphite fine focus sealed tube Mo K$\alpha$ (0.710 73 Å) source. Crystals were mounted on a cryoloop using Paratone-N oil. Data were processed and refined using the program SAINT supplied by Siemens Industrial Automation. Structures were solved by intrinsic phasing methods in SHELXT and refined by standard difference Fourier techniques in the SHELXTL program suite.[80] Hydrogen atoms were located in the difference map and were refined isotropically using a riding model; all non-hydrogen atoms were refined anisotropically. The structure of **3** contains a pentafluorophenyl group that is disordered over two positions in a ratio of ~0.6:0.4, as well as three molecules of disordered THF and one molecule of disordered pentane per molecule of **3**. Since the solvent disorder could not be modeled satisfactorily, the associated electron density was removed using the program SQUEEZE. The structure of **6** contains two molecules of THF, one molecule of *N*-methyl-2-pyrrolidone, and one disordered molecule of pentane per two molecules of **6**. Since the disordered pentane molecule of **6** could not be satisfactorily modeled, this electron density was removed using the program SQUEEZE. Unit cell parameters, morphology, and solution statistics for the structure are summarized in Supporting Information, Table S1. Thermal ellipsoid plots are drawn at the 50% probability level with hydrogen atoms removed for clarity.

## RESULTS

**Corrole Synthesis and Structure.** Bromination of the corrole periphery affords a convenient method of functionalization and a useful synthetic handle for cross-coupling chemistry as a means of further elaboration of the corrole macrocycle.[21,81−87] Compound **2** was prepared by the HCl-catalyzed condensation of dipyrromethane **1** and methyl 4-formylbenzoate (Figure 1), following the procedure of Koszarna and Gryko.[88] This method furnishes corroles in high yield (up to 32% yield for 5,10,15-triphenylcorrole) and facilitates the preparation of *trans*-$A_2B$ corroles without scrambling (i.e., circumventing the formation of the *cis*-$A_2B$ isomer). The desired product was obtained in 51% yield, giving quantities of ~1 g in a typical synthesis. This yield is greatly improved over previous preparative methods,[51] which used TFA as the acid catalyst and gave **2** in 18% yield (~300 mg of isolated product).

An additional fluorescent macrocyclic product, obtained in 17% isolated yield, was assigned as the 3,3′ linked dimer **3** on the basis of mass spectrometry and $^1$H NMR. Seven unique $\beta$-pyrrole protons in the $^1$H NMR spectrum established that the lower-symmetry 2,3′-linked dimer had not formed. The chemical shift of the singlet ($\delta$ 9.16 ppm), attributed to the proton adjacent to the corrole−corrole linkage, suggested a 3,3′ linkage as it compared well to $\delta$ 9.12 ppm for the 3,3′ dimer of 5,10,15-tris(pentafluorophenyl)corrole ($H_3$TPFC).[89] A resonance comparable to that of the 2,2′ dimer of $H_3$TPFC ($\delta$ 9.66 ppm) was also absent,[90] precluding formation of this derivative as a byproduct. $H_3$TPFC has recently been observed to undergo regioselective oxidative coupling in the presence of quinone oxidants to give 3,3′-linked oligomers,[91] thus offering a plausible explanation for the formation of **3** as a byproduct in the preparation of **2**.

Serial bromination of **2** generated brominated corroles **4**−**6**. The majority of bromination reactions have been performed on metallocorroles by using a significant excess of $Br_2$ to deliver the $\beta$-octabromo derivatives.[81−83] A notable exception is germanium corrole, which gave hexabromo, pentabromo, or tribromo derivatives (each as a single regioisomer), depending on the amount of $Br_2$ added.[84] As an alternative to $Br_2$, there has been a report on the bromination of $H_3$TPFC using NBS; the extent of bromination is proportional to the amount of added NBS.[85] Unlike $H_3$TPFC, we find that treatment of corrole **2** with NBS is not straightforward. Addition of small volumes of NBS to **2** prompted the reaction mixture to turn from violet to blue-green, and the observed fluorescence intensity of the solution, as observed using a hand-held UV lamp (365 nm) as the excitation source, dramatically decreased.

In an attempt to better control the distribution of brominated products, the amount of NBS was varied from 1.9 to 2.7 equiv (Figure 1). In all cases, a mixture of products (mono-, di-, and tribromo corroles) was obtained. However, this reaction, as with nearly all corrole peripheral functionalization reactions,[26] is regioselective, producing four unique species: 2-bromo-**2**, 3-bromo-**2**, **4**, and **5**. This result suggests that bromination is not sequential and that all products are formed in the course of the reaction. Indeed, monobromo corroles were identified in reaction mixtures that used more than 3 equiv of NBS. The best results were achieved when using 2.6 equiv of NBS. All of these species have very similar $R_f$ values by thin-layer chromatography (TLC, 1:1 hexanes/$CHCl_3$) and appear as a single spot on the TLC plate. Fortunately, each species has a distinctive color, making it possible to separate these compounds by column chromatography. Compound **5** elutes first as a blue-green solution, followed by **4** as a violet solution with a gold-amber hue (see TOC image). These two products were obtained as pure species by careful column chromatography. The two monobrominated corroles (violet-brown solution) eluted next as a mixture, as identified by $^1$H HMR, along with decomposition products. These late-eluting fractions were discarded because each contained a mixture of several products, as evidenced by multiple methyl ester resonances in the $^1$H HMR spectrum. Monobrominated corrole isomers are inseparable,[85] and therefore no efforts were made to further purify or characterize these compounds, as mixtures are not suitable for photophysical characterization. Small fraction volumes were collected to ensure that pure compounds were isolated. We note that reported yields represent the isolated yields of pure compounds; the actual reaction yields are presumably higher, as fractions identified as mixtures of products were discarded. Compound **6** was isolated as the exclusive product when more than 4 equiv of NBS were used. This suggests that the excess NBS reacts with any remaining corrole with fewer than four bromine atoms to give a single product. Moreover, this result also demonstrates that the unique axis of the corrole (i.e., the 2, 3, 17, and 18 positions) is the most reactive and that excess NBS does not react at the opposite side (i.e., the 7, 8, 12, and 13 positions), a result that is consistent with known corrole reactivity.[26]

Diffraction-quality crystals of compounds **2**, **3**, and **6** were obtained as purple blocks from THF and pentane. The thermal ellipsoid plots of the refined structures are shown in Figures 2, 3, and 4, and a summary of the crystallographic data is presented in Supporting Information, Table S1. The solid-state structure of **2** (Figure 2) exhibits structural metrics that fall within the range observed for other $C_6F_5$-substituted free-base corroles.[19,92,93] Three of the four pyrrole rings are nearly coplanar, while the fourth cants out of the plane and hydrogen bonds with a THF solvent molecule. The macrocycle has a mean deviation of 0.170 ± 0.144 Å from the mean 23-atom plane, with a maximum deviation of 0.501 Å for the pyrrole that participates in hydrogen bonding. The solid-state structure of **3** unambiguously confirms the 3,3′ linkage of the dimer (Figure


DOI: 10.1021/ic502860g
Inorg. Chem. 2015, 54, 2713−2725

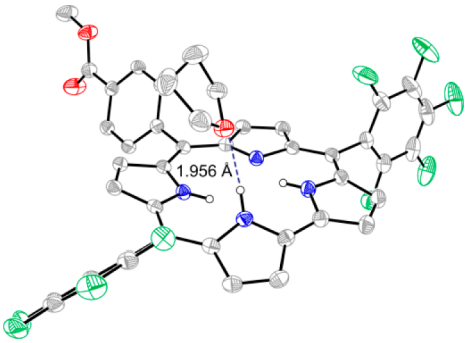


**Figure 2.** Solid-state structure of **2**, showing a THF molecule hydrogen bonded to the corrole core. Thermal ellipsoids are drawn at the 50% probability level, and carbon-bound hydrogen atoms were removed for clarity.

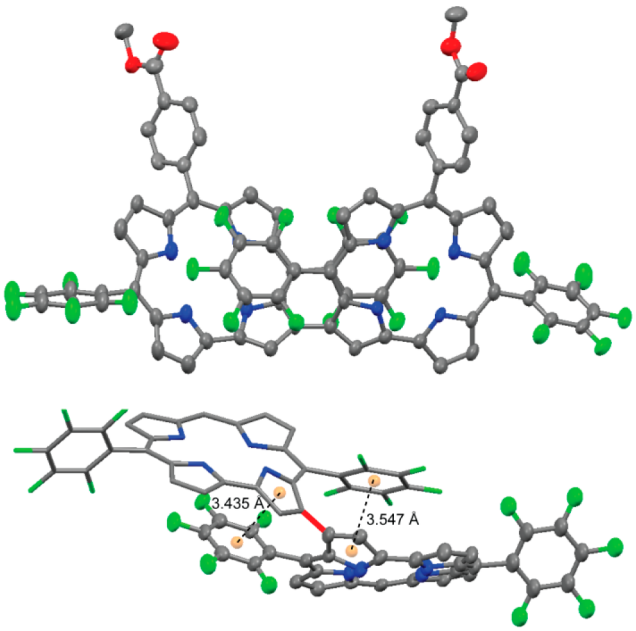


**Figure 3.** Solid-state crystal structure of compound **3**. Thermal ellipsoids are drawn at the 50% probability level. The lower structure highlights the $\pi$-aryl interaction by showing the centroids of the relevant rings and their corresponding distances. To better illustrate this conformation, one corrole unit is drawn with ellipsoids while the other uses capped sticks. Additionally, the 3,3′ linkage is highlighted in red. For clarity, hydrogen atoms and the 10 meso substituents were removed from the lower structure.

3, top). The structure is highly contorted to enable a favorable $\pi$-aryl interaction between a pentafluorophenyl ring and a pyrrole unit of the macrocycle (Figure 3, bottom), giving 3.435 and 3.547 Å distances between the centroids of these rings. This is atypical of meso-aryl corroles and porphyrins, which usually have these substituents orthogonal to the macrocycle plane. This close contact results in a 42.09° separation between the mean 23-atom planes of the corrole units. This is comparable to that observed for the 3,3′-linked dimer of $H_3$TPFC (CCDC No. 842519),[91] which displays a 47.60° separation of the corrole planes. Despite this close contact, the corrole units adopt a highly planar structure, with three of the pyrrole units being largely coplanar, while the fourth pyrrole unit (i.e., the one participating in dimer formation) cants out of the corrole plane. The crystal structure of **6** displays two corroles in the asymmetric unit that display differing degrees of

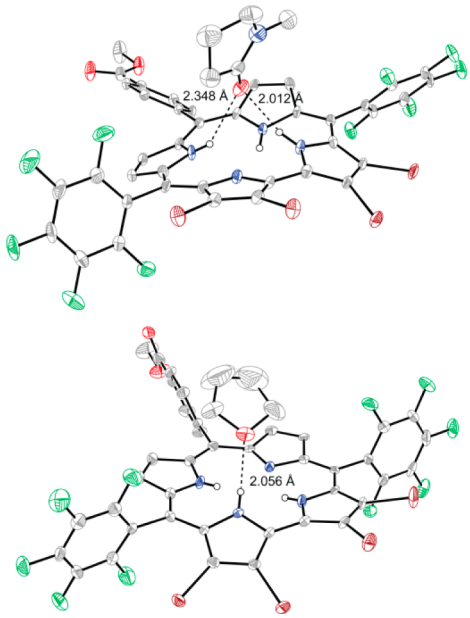


**Figure 4.** Solid-state crystal structure of compound **6** showing the two independent corrole molecules in the asymmetric unit. Thermal ellipsoids are drawn at the 50% probability level, and carbon-bound hydrogen atoms were removed for clarity. One corrole is highly nonplanar, exhibiting a molecule of *N*-methyl-2-pyrrolidone bound to the core (upper), while the other corrole (lower) features a hydrogen bonded THF molecule, akin to the structure of **2** (Figure 2).

nonplanarity. One molecule (Figure 4, top) is highly nonplanar, exhibiting a mean deviation of 0.259 ± 0.214 Å from the mean 23-atom plane, with a maximum deviation of 0.639 Å (a pyrrole carbon bearing a bromine atom). This large deviation may originate from a crystal packing effect, as this molecule has a molecule of *N*-methyl-2-pyrrolidone hydrogen bonded to the macrocycle core. Two pyrrole units cant out of the plane to result in this large deviation from planarity. Conversely, the other corrole (Figure 4, bottom) has a THF molecule hydrogen bonded to the macrocycle core; it exhibits mean deviation of 0.126 ± 0.111 Å from the mean 23-atom plane, with a maximum deviation of 0.388 Å (a pyrrole carbon bearing a bromine atom). This observation is consistent with what is observed in the solid-state structure of **2** and may be more representative of corrole conformations.

**Absorbance Spectroscopy.** The electronic absorption spectra of corroles **2**, **4**, **5**, and **6**, which are shown in Figure 5a, exhibit intense Soret or B bands in the near-UV and weaker Q bands in the visible spectral regions. Supporting Information, Table S2 lists the absorbance maxima for these compounds. The Soret band of **2** is quite broad (43 nm fwhm), and the line shape displays a plateau rather than a Gaussian profile, suggestive of overlapping transitions (i.e., $B_x$ and $B_y$ polarizations), which is expected for lower-symmetry corrole molecules. With the inclusion of two bromine atoms along the same face of the corrole (compound **4**), the Soret red-shifts by 3 nm and broadens (46 nm fwhm), establishing that the $B_x$ and $B_y$ transitions are energetically more separated upon bromination. Sequential bromination further separates these transitions such that the two bands are clearly resolved in **6** (Supporting Information, Figure S1a). In this progression of compounds, the edge defined by the 2, 3, 17, 18 positions of the molecule is perturbed, while the other edge (2, 3, 7, 8 positions) is much less perturbed. For clarity, the *y* axis is taken


DOI: 10.1021/ic502860g
*Inorg. Chem.* 2015, 54, 2713−2725

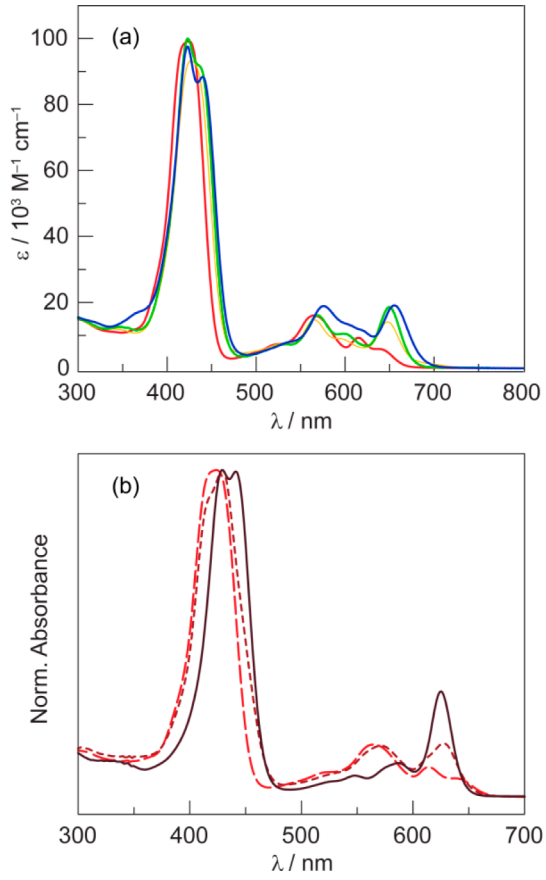


**Figure 5.** (a) Comparison of the steady state absorption spectra of a series of corroles in toluene: **2** (red —), **4** (yellow —), **5** (green —), and **6** (blue —). With an increasing extent of bromination, the Soret band splits, and these transitions exhibit a spectral red shift. See Supporting Information, Figure S1 for an expansion of the Soret and Q-band regions. (b) Steady-state absorption spectra of **2** in toluene (red – –), PhCN (maroon - - -), and DMSO (purple —).

as the $C_2$ pseudorotational axis and is aligned through the 10 position, whereas the *x* axis is perpendicular to it in the plane of the corrole and passes through the 5 and 15 positions.

All four corroles exhibit four Q bands in the 500–700 nm region. Consistent with what is observed for porphyrins, there are two fundamental bands $Q_x(0,0)$ and $Q_y(0,0)$ at 565 and 650 nm, respectively, each with vibrational overtones $Q_x(1,0)$ and $Q_y(1,0)$ at 530 and 600 nm, respectively (Supporting Information, Figure S1b). This nomenclature is in line with that used to describe porphyrin transitions. An energy difference of ~1200–1350 $cm^{-1}$ is observed for each Q(1,0) and Q(0,0) pair in this series of molecules, with an average energy separation of 1277 $cm^{-1}$ ± 63 $cm^{-1}$; this is consistent with the energy separation of ~1250 $cm^{-1}$ observed for porphyrins.[94] Additionally, there is an energy spacing of ~2100–2200 $cm^{-1}$ between corresponding *x* and *y* bands (i.e., $Q_x(0,0)$ and $Q_y(0,0)$) with an average separation of 2148 $cm^{-1}$ ± 64 $cm^{-1}$. The splitting of *x* and *y* Q bands is ~3000 $cm^{-1}$ for porphyrins, and this separation is known to be smaller for other tetrapyrrolic macrocycles.[94]

While the *x* and *y* polarizations of these compounds should be distinguished as a result of symmetry, the Soret band of corroles does not typically reflect an (*x*, *y*) polarization, and a single, sometimes broad, absorption feature is observed, as in the case of **2**. The Soret band clearly resolves to two distinct peaks when the compound is dissolved in solvents of increasing dielectric constant (Figure 5b), as has also been observed for both 5,10,15-triphenylcorrole ($H_3$TPC) and 5,10,15-tris(4-methoxyphenyl)-corrole ($H_3$TMPC).[43]

The steady-state absorbance spectrum of dimer **3** (Figure 6) is comparable to the monomeric corroles, except the optical

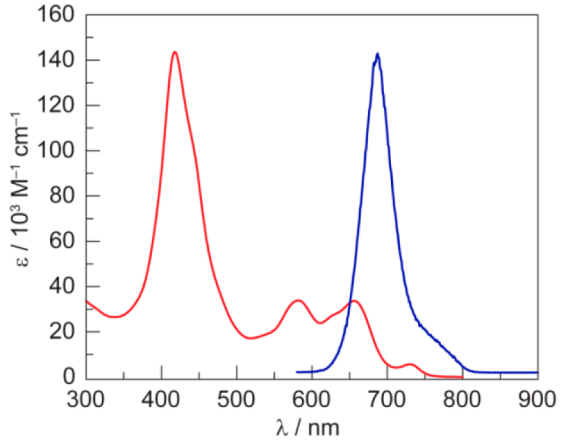


**Figure 6.** Steady-state absorption (red) and emission (blue) spectra ($\lambda_{exc}$ = 560 nm) of dimer **3** in toluene. Qualitatively, these spectra are similar to that of the monomer **2**, but the transitions are more intense; an additional feature at ~750 nm is observed, indicative of a dimeric structure.

absorption transitions are considerably more intense than the corrole monomer. This increased optical absorbance is due to the presence of two fluorophores in a single molecule. The Soret band displays a shoulder, indicative of two overlapping transitions. The most intense peak of **3** is blue-shifted by 338 $cm^{-1}$ relative to **2**. Conversely, all of the Q transitions of **3** are red-shifted relative to **2**: 517 and 766 $cm^{-1}$ for $Q_y$ transitions and 311 and 381 $cm^{-1}$ for $Q_x$. Additionally, compound **3** exhibits a feature at 731 nm ($\varepsilon$ = 5700 $M^{-1}$ $cm^{-1}$) that is unique to a dimeric structure. A similar feature has been observed for corrole dimers and higher order oligomers,[89,91] and it is likely due to transitions between corrole subunits.

**Fluorescence Spectroscopy.** Steady-state emission spectra ($\lambda_{exc}$ = 440 nm) were recorded for toluene solutions of compounds **2**, **4**, **5**, and **6**. Table 1 summarizes the emission data for these corroles, and Figure 7a displays the normalized emission spectra, which exhibit an intense band with a vibrational shoulder to the red; expansion of the Q-band region for compound **2** is presented in Supporting Information, Figure S2. On the basis of the assignment of the Q-band absorption profile, the intense fluorescence band is assigned to $Q_x(0,0)$, and the shoulder is assigned to $Q_x(0,1)$. This nomenclature is consistent with that used to describe fluorescence transitions for free-base porphyrins.[94] A constant energy gap of ~1300–1400 $cm^{-1}$ between $Q_x(0,0)$ and $Q_x(0,1)$ is observed, with an average separation of 1335 $cm^{-1}$ ± 32 $cm^{-1}$, which is comparable to that observed between $Q_x(0,0)$ and $Q_x(1,0)$ in the absorption spectra. The observed Stokes shift between the $Q_x(0,0)$ absorption and emission features is ~400 $cm^{-1}$ for **2**, **4**, and **5**, whereas that of **6** is ~650 $cm^{-1}$. Paralleling trends in the absorption profile, the emission spectra exhibit a red shift with increasing bromination. As observed for the absorbance Q bands, the steady-state emission Q features for **3** are red-shifted relative to **2** by 644 and 795 $cm^{-1}$ for $Q_x(0,0)$ and $Q_x(0,1)$, respectively. The fluorescence quantum


DOI: 10.1021/ic502860g
Inorg. Chem. 2015, 54, 2713–2725

**Table 1. Photophysical Data for Free-Base Corroles**

| corrole[a] | $Q_x(0,0)^b$ | $Q_x(0,1)^b$ | $\tau_o{}^c$ (ps) | $\Phi_f{}^d \times 10^2$ | $k_r{}^e$ ($s^{-1}$) | $k_{nr}{}^e$ ($s^{-1}$) |
|---|---|---|---|---|---|---|
| **2** | 657 | 722 | 4111 ± 24[f] | 15 | $4.06 \times 10^7$ | $2.30 \times 10^8$ |
| **4** | 664 | 728 | 235 ± 7 | 1.1 | $4.74 \times 10^7$ | $4.26 \times 10^9$ |
| **5** | 668 | 732 | 121 ± 3 | 0.51 | $4.15 \times 10^7$ | $8.10 \times 10^9$ |
| **6** | 684 | 770 | 84 ± 3 | 0.47 | $5.66 \times 10^7$ | $1.20 \times 10^{10}$ |
| **3** | 686 | 766 | 3285 ± 20 | 27 | $8.86 \times 10^7$ | $2.40 \times 10^8$ |

[a]Toluene solution, transition wavelengths are in units of nm. [b]Observed transitions with $\lambda_{exc}$ = 440 nm. [c]Freeze–pump–thawed samples (<$10^{-4}$ Torr) with $\lambda_{exc}$ = 400 nm. [d]Fluorescence quantum yield, relative to $H_2$TPP in toluene ($\phi_f$ = 0.11). [e]Calculated using eq 3. [f]95% confidence interval.

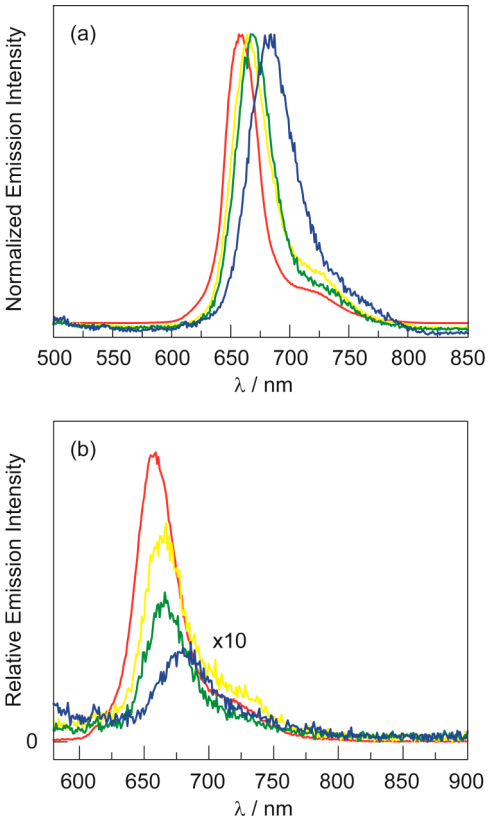


**Figure 7.** Steady-state emission for a series of corroles in toluene: **2** (red), **4** (yellow), **5** (green), and **6** (blue). (a) Normalized steady-state emission spectra ($\lambda_{exc}$ = 440 nm), demonstrating a red shift in the emission maximum. (b) Absorbance-matched ($A_{560}$ = 0.100 ± 0.002) emission spectra ($\lambda_{exc}$ = 560 nm), reflecting fluorescence quenching upon bromination. For clarity, the emission intensity of compounds **4**, **5**, and **6** was increased by a factor of 10.

yield also exhibits a pronounced decrease with increasing bromination. Figure 7b shows the steady-state emission spectra ($\lambda_{exc}$ = 560 nm) for absorbance-matched toluene solutions of **2**, **4**–**6** at the excitation wavelength of $\lambda_{exc}$ = 560 nm ($A_{560}$ = 0.100 ± 0.002). The fluorescence quantum yields are provided in Table 1, where eq 1 was used to determine Φ with $H_2$TPP in toluene as the reference ($\Phi_{ref}$ = 0.11). No phosphorescence was observed from the triplet manifold of these corroles.

Consistent with emission intensity results, the emission lifetime also exhibits a marked decrease with bromination. The fluorescence lifetimes of nonbrominated corroles listed in Table 1 were determined from fitting the data with a monoexponential decay ($R^2$ > 0.99). For the brominated derivatives, the lifetimes were so short that the decay is on the order of the instrument response function, as illustrated in Supporting Information, Figure S3. As a result, these traces were fit with an exponential-modified Gaussian ($R^2$ > 0.99). Using eq 3, the radiative and nonradiative rate constants $k_r$ and $k_{nr}$, respectively, may be determined for each compound:

$$\Phi = \frac{k_r}{k_r + k_{nr}} = k_r\tau \tag{3}$$

where Φ is the is emission quantum yield, and $\tau$ is the natural fluorescence lifetime. Whereas $k_r$ is effectively invariant for all monomeric corroles, $k_{nr}$ increases significantly with bromination. Although the quantum yield of **3** is nearly twice that of **2**, the radiative lifetime is similar, indicating that additional deactivation pathways are present in the dimer.

**Transient Absorption Spectroscopy.** In the absence of phosphorescence, nanosecond transient absorption (TA) was utilized to probe the spectral features of the triplet state and its relaxation dynamics. The TA spectra of corroles **2** and **4**–**6** in toluene, shown in Figure 8 for aerated samples and Supporting Information, Figures S4–S7 for freeze–pump–thawed (fpt) samples, were recorded by pumping the Soret band of the ground state absorption spectrum ($\lambda_{exc}$ = 430 nm). The spectral data is summarized in Table 2. The TA spectra are dominated by bleaches of the ground state Soret and Q bands with a concomitant growth of two features: one centered at ~380 nm and the other at ~470 nm. The normalized triplet absorption spectra of compounds **2** and **4**–**6** is presented in Supporting Information, Figure S8. The two major features in the spectrum red shift upon bromination, although the observed differences among the brominated derivatives **4**–**6** are nominal. This suggests that the nature of the triplet state is quite similar across this series of corroles. Consistent with trends from the ground state electronic absorption spectrum, the higher energy band of **3** in the TA spectrum (Supporting Information, Figures S9 and S10) is nominally (~140 $cm^{-1}$) blue-shifted whereas the lower energy band around 505 nm is significantly red-shifted (~1660 $cm^{-1}$) relative to that observed for **2**.

The temporal evolution of the TA spectra was determined from monitoring single wavelength kinetics for the prominent spectral feature at ~470 nm for each species. Lifetime data are given in Table 2. Compounds **4**–**6** obey monoexponential decay kinetics ($R_{adj}{}^2$ > 0.99) whereas **2** and **3** exhibit biexponential decay kinetics with the shorter lifetime component dominating the fit. The biexponential decay indicates the presence of two distinct triplet states for **2** and **3**. The lifetime of the triplet excited state decreases with increasing bromination. Introduction of oxygen into solution leads to significant quenching of the long-lived triplet feature in all samples. The decreased lifetime furnishes a diffusional rate constant ($k_q \approx 2 \times 10^{-9}$ $M^{-1}$ $s^{-1}$) for the quenching of the triplet excited state by oxygen.

**Density Functional Theory Calculations.** DFT calculations were performed using the B3LYP functional to gain insight into the nature of the electronic structure and the effect


DOI: 10.1021/ic502860g
Inorg. Chem. 2015, 54, 2713–2725

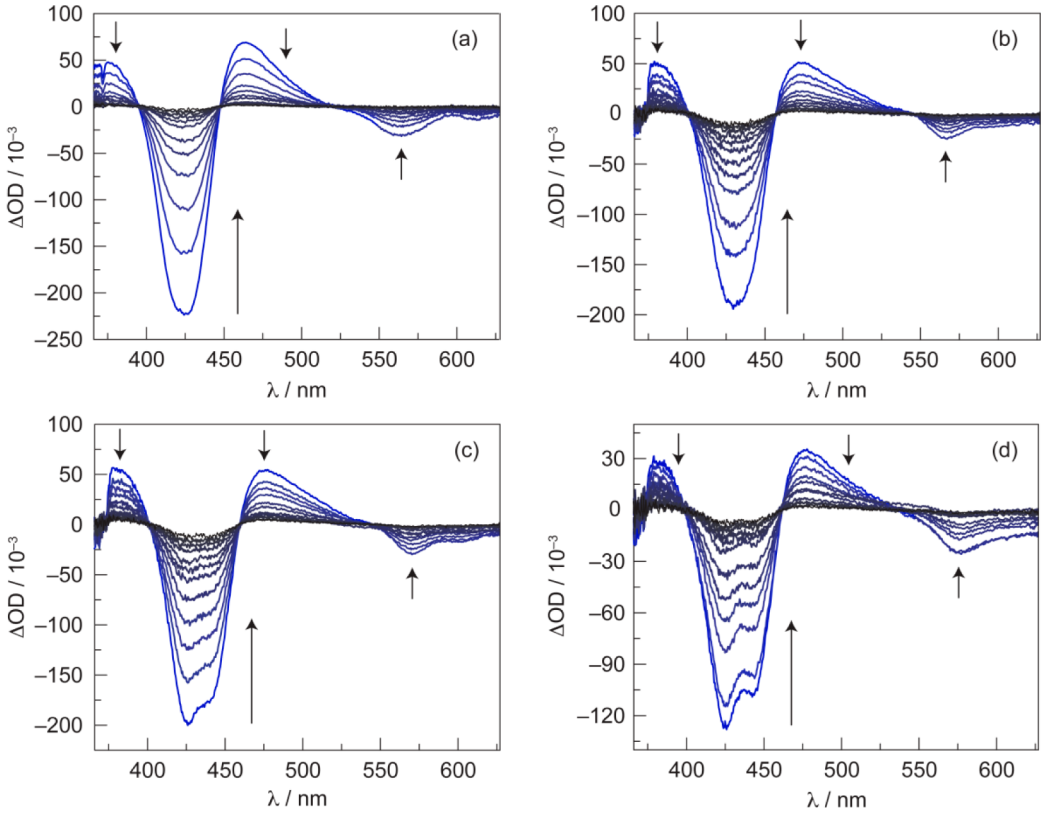


**Figure 8.** Nanosecond transient absorption (TA) spectra ($\lambda_{exc}$ = 430 nm) of aerated toluene solutions of (a) **2**, (b) **4**, (c) **5**, and (d) **6**, showing the bleach of the ground state with concomitant growth of the triplet state. The temporal evolution of each spectrum is from 20 to 735 ns in 65 ns intervals. The corresponding spectra of fpt samples are presented in Supporting Information, Figures S4−S7.

**Table 2. Summary of Transient Absorption Kinetics Data for Corroles**

| corrole[a] | $Abs_1$[b] | $Abs_2$[b] | $\tau_{o1}$[c] ($\mu$s), %[d] | $\tau_{o2}$ ($\mu$s), %[d] | $\tau_{air}$ (ns) | $k_q$ ($M^{-1}$ $s^{-1}$) |
|---|---|---|---|---|---|---|
| **2** | 377 | 465 | 151 ± 5[e] (21) | 19.2 ± 0.6 (79) | 230 ± 3 | $2.2 \times 10^9$ |
| **4** | 385 | 470 | 12.2 ± 0.1 (100) | | 263 ± 3 | $1.9 \times 10^9$ |
| **5** | 384 | 474 | 8.8 ± 0.1 (100) | | 283 ± 5 | $1.8 \times 10^9$ |
| **6** | 382 | 473 | 5.4 ± 0.1 (100) | | 298 ± 2 | $1.6 \times 10^9$ |
| **3** | 375 | 504 | 88.3 ± 9.1 (29) | 22.8 ± 1.3 (71) | 267 ± 5 | $1.9 \times 10^9$ |

[a]Toluene solution, transition wavelengths are in units of nm. [b]Measured from transient absorption spectra with $\lambda_{exc}$ = 430 nm. [c]Freeze−pump−thawed samples (<$10^{-4}$ Torr). [d]Relative contribution to the biexponential fit. [e]95% confidence interval.

of bromination on the frontier molecular orbitals. Ground-state geometry optimization for compounds **2** and **4**−**6** was carried out using the 6-311G** basis set and a CPCM solvation model in toluene. The optimized structures, which are presented in Supporting Information, Figures S11−S14 with the Cartesian coordinates listed in Supporting Information, Tables S3−S6, were verified as local minima by performing frequency calculations and ensuring that there were no imaginary frequencies. Qualitatively, the structures are quite similar and exhibit a single pyrrole ring (the so-called A or D ring) that largely deviates from the mean 23-atom plane, irrespective of bromination. The calculated structure of **2** is consistent with the solid-state structure of **2** and other free-base corroles, as typified by $H_3$TPFC.[19,92,93] In these crystal structures, three of the pyrrole units are nearly coplanar while the fourth (the A or D ring) cants out of the plane. The root-mean-square (RMS) deviation between the calculated and solid-state structures of **2** is 0.430 Å; the overlay of the structures is presented in Supporting Information, Figure S15. Although the calculated distortion of the macrocycle upon bromination is not as pronounced as it is in the crystal structure (Figure 4, top), the solid-state (Figure 4, bottom) and calculated structures of **6** are quite similar (Supporting Information, Figure S16), with an RMS deviation of 0.566 Å. This larger deviation relative to **2** is primarily due to a different conformation of the 10-meso substituent rather than the corrole ring itself.

The frontier molecular orbitals of the corroles (HOMO−1, HOMO, LUMO, and LUMO+1) are shown in Figure 9 for **2** and Supporting Information, Figures S17−S19 for **4**−**6.** Qualitatively, the frontier orbitals are all $\pi$-type symmetry with significant orbital density at the $\beta$ positions. The LUMO and HOMO−1 orbitals possess the greatest amount of density at the $\beta$ positions, suggesting that these two orbitals are most affected by $\beta$ substitution. As shown in Supporting Information, Figure S20 and Table S7, the frontier orbitals are energetically well-separated from the rest of the molecular orbital manifold. The calculated HOMO−LUMO gap decreases with increasing bromination, consistent with the observed red shift of spectral features: 2.51 eV (494 nm) for compound **2** to 2.43 eV (510 nm) for compound **6** (see Supporting Information, Table S7).


DOI: 10.1021/ic502860g
Inorg. Chem. 2015, 54, 2713−2725

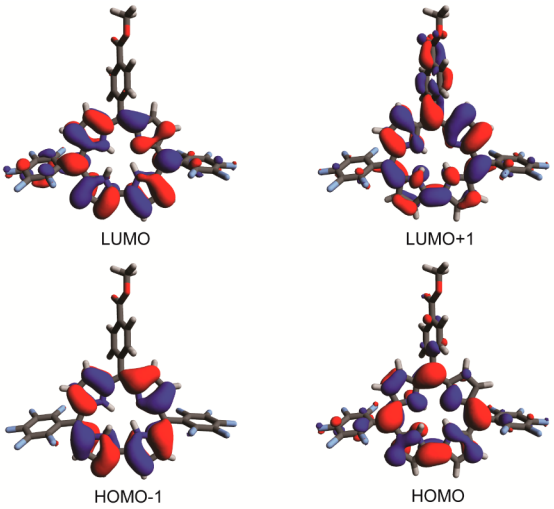


**Figure 9.** Four frontier molecular orbitals calculated for compound **2**, illustrating that all four orbitals possess electron density at the $\beta$ positions.

Whereas the trend is captured, the absolute values of the calculated HOMO−LUMO gap deviate from the observed energies of the lowest-energy electronic transitions. Conversely, the observed and calculated spectra are in better agreement with TD-DFT calculations (vide infra).

The ground-state geometry optimization of the dimer **3** was performed as a full molecule without truncation (presented in Supporting Information, Figure S21 and Cartesian coordinates in Supporting Information, Table S8) and validated as a local minimum by a frequency calculation. The calculated structure displays a more splayed geometry than that of the solid-state structure, with a 65.46° separation between the mean 23-atom planes of the corrole (as compared to 42.09° of Figure 3). The $\pi$-aryl interaction of the pentafluorophenyl and pyrrole rings is not captured in the calculation, with a 4.119 Å distance between the centroids of these rings (compared to 3.435 Å in Figure 3). This results in a longer center-to-center distance of the corrole macrocycles: 9.199 Å for the computed structure compared to 8.304 Å for the solid-state structure. The molecular orbitals of **3** are similar to those of the monomer **2** (Supporting Information, Figure S22), although there are two dimer orbitals per monomer orbital owing to the presence of two distinct $\pi$ systems in the dimer. As a result, there are eight frontier orbitals that are analogous to the four orbitals for monomeric corroles. The two nearly degenerate orbitals only differ by the nature of the lobe along the 3−3′ bond that forms the dimer (see Supporting Information, Figures S23 and S24). For example, the only difference between HOMO−3 and HOMO−2 of **3** is the nature of the lobe along the 3−3′ bond: the HOMO−3 has a continuous lobe, whereas the HOMO−2 has a node along the bond. This phenomenon is observed for each pair of molecular orbitals in the dimer **3**.

TD-DFT calculations were performed using the B3LYP functional to interrogate the nature of the excited states of these compounds and correlate the electronic structure to the absorption spectra. Single-point excited-state energy calculations determined the 10 lowest-energy singlet and triplet states for compounds **2**, **4**−**6** using the 6-311++G** basis set and a CPCM solvation model in toluene. Simulated UV−vis spectra of these compounds are presented in Supporting Information, Figures S25−S28. The energy of these singlet and triplet excited states, as well as the orbital contributions to each transition, are presented in Supporting Information, Tables S9−S16. The four lowest-energy singlet excited states give rise to two Q-like transitions and two Soret-like transitions. These states ($S_1$−$S_4$) for compounds **2**, **4**−**6** exclusively involve the four frontier orbitals (with the exception of $S_4$ for **6**, which has an 18% contribution of HOMO−2 → LUMO). The deviation between the calculated and experimental optical transitions range from 0.05 to 0.28 eV and is in range with TD-DFT benchmark studies on test sets of organic molecules, which demonstrate an absolute mean error of 0.3−0.5 eV.[95−97] Although the exact energies of the calculated transitions do not align precisely with experiment, the predicted UV−vis spectra (Supporting Information, Figures S25−S28) qualitatively reflect experimental observations. The Soret region broadens and subsequently splits with increasing bromination. As observed experimentally, the Soret bands of **2** and **4** look like a single, broad transition, while **5** displays a prominent shoulder, and **6** exhibits two resolved transitions. Additionally, the oscillator strength of the lower-energy Q-band increases with increasing bromination, as observed experimentally. Moreover, the two Q states ($S_1$ and $S_2$) and two Soret states ($S_3$ and $S_4$) are orthogonally polarized (see Supporting Information, Tables S17−S20 for the components of the electronic dipole moment vectors for states $S_1$−$S_4$). This implies that both the Q and B bands are split into $x$ and $y$ polarizations due to the low symmetry of the corrole. Thus, the split Soret band is due to the energetic separation of the $B_x$ and $B_y$ transitions. Calculated triplet states are qualitatively similar to absorbance bands observed experimentally by TA spectroscopy (see Supporting Information, Figure S8), although the exact wavelength maxima are slightly shifted.

To interrogate the nature of the excited states of **3**, TD-DFT calculations were performed. Single-point excited-state energy calculations were performed to determine the 15 lowest-energy singlet and triplet states using the same methods as those used with compounds **2** and **4**−**6**. The simulated UV−vis spectrum is presented in Supporting Information, Figure S29 and the results of these calculations are summarized in Supporting Information, Tables S21−S23. Since the dimer has twice the number of molecular orbitals and they come in nearly degenerate pairs, there are many more states calculated for this compound. For example, 15 singlet states appear in the 630 to 390 nm range, whereas there are only four for the monomeric compounds **2** and **4**−**6**. Thus, it is not surprising that there are several nearly degenerate states calculated for the dimer. This phenomenon is particularly prevalent for the triplet states. Despite the preponderance of states, there are only four Q-like states and four Soret-like states that have substantial (>0.05) oscillator strengths, giving a qualitative correspondence to experimental observations.

## DISCUSSION

Since the introduction of one-pot corrole synthetic methodologies,[18−21] there has been a renewed interest in corrole chemistry with regard to the coordination chemistry, reactivity, and applications of these molecules. Given the diverse and numerous reports of corroles, $H_3$TPFC has become the archetypical corrole, just as 5,10,15,20-tetraphenylporphyrin ($H_2$TPP) is the prototypical porphyrin. The corrole core is inherently more electron-rich than porphyrin[98] and, hence, is particularly prone to decomposition by prolonged exposure to light and oxygen. In this regard, $H_3$TPFC has three electron-


DOI: 10.1021/ic502860g
Inorg. Chem. 2015, 54, 2713−2725

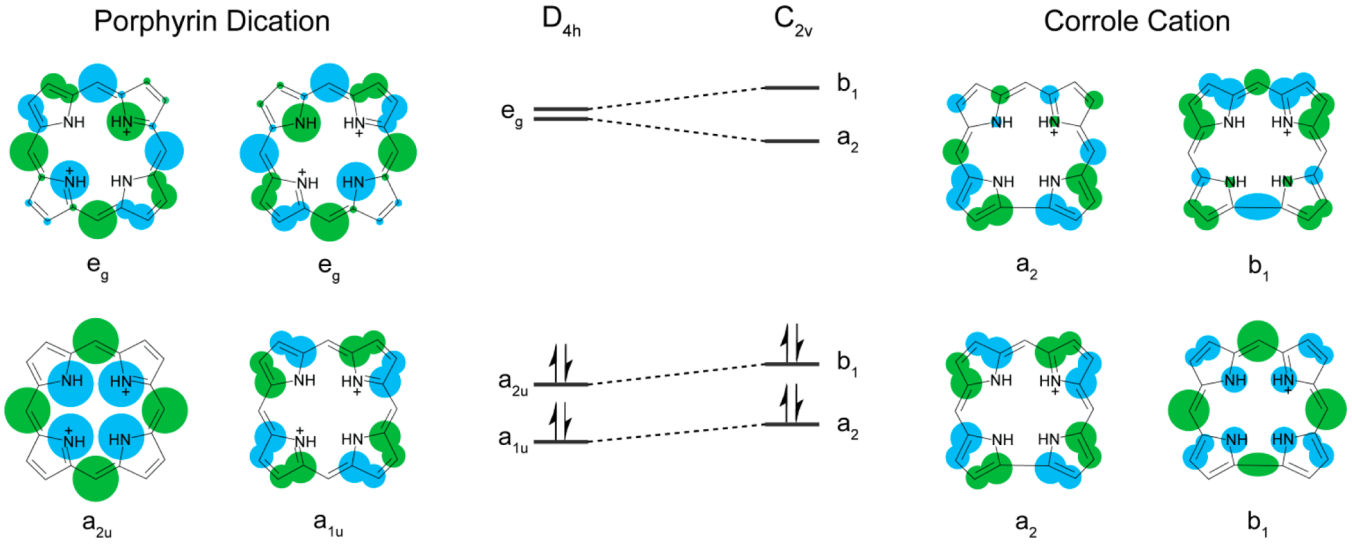


**Figure 10.** The four frontier orbitals for a porphyrin with $D_{4h}$ symmetry, adapted from ref 94. With a descent in symmetry from porphyrin with $D_{4h}$ symmetry to corrole with $C_{2v}$ symmetry, the degeneracy of the LUMOs is lifted. The schematics for the corrole frontier orbitals are adapted from DFT calculations reported in refs 103 and 104; the orbital ordering is based on the calculations shown in Figure 9 and ref 105.

withdrawing pentafluorophenyl groups to reduce the electron density of the tetrapyrrole core, rendering this molecule one of the most stable (i.e., resistant to decomposition) corroles.[99] To harness the stability of $H_3$TPFC while still featuring a synthetic handle for further derivatization or conjugation, we targeted the preparation of corrole **2** and its brominated analogues. This molecule features two pentafluorophenyl groups for stability as well as a methyl ester that may be hydrolyzed to a carboxylic acid, which may subsequently react with a free amine to furnish more elaborate molecular architectures via amide bond formation.

*β*-Substitution on the pyrrole units of the corrole ring significantly perturbs the electronic structure by modulating the relative energies of the HOMO and LUMO levels. A convenient benchmark for the corrole electronic structure is the four orbital model of porphyrins shown in Figure 10.[94,100−102] The two HOMOs ($a_{1u}$ and $a_{2u}$) and the two LUMOs ($e_g$) of $\pi$ symmetry are energetically well-separated from all other molecular orbitals. Transitions associated with the ($a_{2u}e_g$) and ($a_{1u}e_g$) electron configurations, which are $\pi-\pi^*$ in nature, lead to the characteristic Soret and Q bands. Ghosh and co-workers have demonstrated that this four orbital model holds for corroles as well.[103,104] With a descent in symmetry from $D_{4h}$ for a metalloporphyrin to $C_{2v}$ for a metallocorrole, the $x$ and $y$ axes of the molecule are inequivalent, resulting in splitting of both the Q and B bands into $x$ and $y$ components. Symmetry is further lowered for free-base corroles with their three interior N−H protons. The four lowest-energy transitions (in $C_{2v}$ symmetry) are ($b_1b_1$) and ($a_2a_2$) of $A_1$ symmetry, as well as ($b_1a_2$) and ($a_2b_1$) configurations of $B_2$ symmetry;[103] they configurationally mix to result in intense B bands and weak Q bands, analogous to those observed for porphyrins. Orbital calculations of an unsubstituted gallium(III) corrole[103] and diboron corrole[104] indicate that all four frontier orbitals possess some electron density at the *β*-positions. The order of the orbitals is consistent with the DFT calculations of Figure 9, as well as the experimental electron paramagnetic resonance spectrum of an oxidized Ga(III) corrole. This species displays hyperfine coupling to the nitrogen atoms, demonstrating that the unpaired electron resides in an orbital with density on the nitrogen atoms, thus supporting the assignment of the HOMO as the orbital of $b_1$ symmetry (Figure 10) and the HOMO−1 of $a_2$ symmetry.[105]

The series of compounds **2** and **4**−**6** provides insight into the correlation of the absorption spectra with the molecular orbital picture of Figure 10. A unique feature of corroles is the observance of the splitting of the Soret into two bands under various experimental conditions. Deprotonation of a pyrrole nitrogen has been implicated as the origin of this phenomenon in polar solvents.[18,20,43,92,106] However, there are several counterexamples in which a split Soret band is observed in nonpolar solvents such as toluene or dichloromethane.[40,107] In the case of **2**, two bands do resolve with increasing polarity of the solvent (Figure 5b). However, a very strong acid would be formed if solvent were to deprotonate the macrocycle (e.g., $pK_a(PhCNH^+) = -10$).[108] Alternatively, unique Soret transitions have been ascribed to the presence of two tautomers in solution.[47,92,107] While tautomerization is fast at room temperature on the NMR time scale,[109] the energy difference between tautomers is too small ($E_{S0}$ = 33 cm$^{-1}$) to account for the 970 cm$^{-1}$ observed splitting.[47] Moreover, DFT calculations have demonstrated that each tautomer displays several Soret-like transitions.[107] Finally, it has been postulated that the split Soret may be ascribed to nonplanarity of the macrocycle, engendered by sterically demanding meso substituents,[40,110] though corroles with unhindered substituents also exhibit a split Soret band.[107] Supporting Information, Table S24 provides structural metrics to assess the planarity of meso substituted free-base corroles without *β* substituents. The example with mesityl substituents, which has the smallest deviation from the 23-atom plane and the smallest dihedral angles of Table S24, displays a split Soret band in toluene.[111] Conversely, corroles with pentafluorophenyl groups do not exhibit split Soret bands although they display a greater degree of nonplanarity.[112,113] As a result, there is no strong correlation between the degree of nonplanarity and splitting of the Soret band. A better correlation is the asymmetry induced along the $x$ and $y$ axes of the corrole macrocycle. Differentiation of the $x$ and $y$ axes, either by structural distortion of the macrocyclic ring, or more directly by chemical substituents, leads to an energetic


DOI: 10.1021/ic502860g
Inorg. Chem. 2015, 54, 2713−2725

separation of the $x$ and $y$ polarized transitions, manifesting in a resolved split of the Soret band. In the cases of **2** and **4**–**6**, this differentiation is afforded by the bromination of one edge of the corrole. More subtle effects can also influence the polarization as well. As shown by the crystal structures of **2** and **6**, polar solvents may interact with the pyrroles of the corrole to lower the overall symmetry of the system, thus also engendering differences in the transition dipoles along the molecular $x$ and $y$ axes.

The differentiation of the ($x$, $y$) transition dipole moments is also reflected in the Q transitions. The lowest-energy Q(0,0) band is the most perturbed by bromination, exhibiting a significant red shift (358 $cm^{-1}$ in going from **2** to **6**) with a concomitant increase in oscillator strength. This is contrasted with the higher-energy Q(0,0) band, which has similar energy and oscillator strength for **2**, **4**, and **5**, with significant changes only observed for **6**. If the brominated edge of the macrocycle is taken as the $x$ axis (2, 3, 17, 18 positions), then the low-energy Q-band (~650 nm) is consistent with a $Q_x(0,0)$ assignment, as it is most affected by bromination, whereas the higher-energy Q-band (~565 nm) is less affected and is assigned as $Q_y(0,0)$. Similarly, the higher-energy band in the Soret manifold is less perturbed, whereas the lower-energy band shifts to lower energy with increasing bromination. These results are consistent with a $y$-polarized higher-energy band and an $x$-polarized lower-energy band. These band assignments are consistent with the results of magnetic circular dichroism spectroscopy.[107]

Calculated orbital energies are in accordance with the contentions deduced from spectroscopic trends. TD-DFT calculations corroborate that the visible absorbance bands arise from transitions among the four frontier orbitals of Figure 9; the calculated singlet states for **3** constitute transitions among the analogous eight frontier molecular orbitals of the dimer. Although the predicted spectra are qualitatively similar to experiment, the calculations do not accurately predict the low-energy Q bands. A single reference method thus does not account for the significant configuration interaction among the frontier MO set, and as a result, multireference methods[114] are needed to capture the excited states more accurately.

Using the calculated molecular orbitals, one may attempt to correlate electron density with the observed product distribution. Bromination by NBS may proceed by either an electrophilic aromatic substitution (EAS) or radical mechanism. If the EAS mechanism is operative, then the corrole HOMO is likely to participate in the reaction. Conversely, the corrole LUMO may be more prominent in a radical mechanism. This orbital has similar density at the 2 and 3 positions (Figure 9) and may explain the observance of both 2-bromo-**2** and 3-bromo-**2**. The radical mechanism is consistent with the observance of a distribution of products when less than 4 equiv of NBS is used. While this correlation is satisfying, no experiments were performed to determine which mechanism (or if both) is operative in the bromination reaction, and thus a correlation between molecular orbital density and reactivity is tenuous at best.

Emission spectral features red shift with increasing bromination. Calculations clearly establish that the primary orbital contribution in the fluorescence emission is LUMO → HOMO. The difference in the HOMO/LUMO gap between compounds **2** and **6** (640 $cm^{-1}$) is quite similar to the observed energy difference (600 $cm^{-1}$) of the $Q_x(0,0)$ emission feature for **2** and **6**. Of greater significance is the substantial decrease in fluorescence quantum yield with bromination. On the basis of lifetime data and the natural lifetimes per eq 3, $k_r$ is relatively constant across the series (~$4 \times 10^7$ $s^{-1}$) for **2** and **4**–**6**, whereas there is a drastic increase in $k_{nr}$ from $2 \times 10^8$ $s^{-1}$ for **2** to $1 \times 10^{10}$ $s^{-1}$ for **6**. Analysis of $\ln(k_{nr})$ versus $\Delta E$ reveals that that the nonradiative rate deviates positively from the linear prediction of the energy gap law (Supporting Information, Figure S30).[115,116] The energy gap law underestimates $k_{nr}$ by a factor of ~10 per bromine atom. Thus, the perturbation of the energy of the frontier molecular orbital manifold by $\beta$-substitution is insufficient to rationalize the significant increase in $k_{nr}$ with bromination. The enhanced $k_{nr}$ is ascribed to a bromine heavy atom effect; increased spin–orbit coupling with increased bromination promotes intersystem crossing and thus results in a shorter emission lifetimes and lower quantum yields. In the absence of bromination, $k_{nr}$ is well-behaved. These results are in accordance with those of Gross and co-workers[54] who observe a serial red shift of spectral features and a decrease in fluorescence lifetime with increasing $\beta$-iodination of aluminum and gallium corroles. Dimer **3** has approximately the same nonradiative rate constant $k_{nr}$ as monomer **2**. The higher fluorescence quantum yield of **3** is in line with an increase in the radiative rate constant ($\tau_o = 1/k_r + k_{nr}$), as reflected by the increased oscillator strength of the dimer.

The photophysical properties of these free-base corroles form a reference for the properties of the corresponding metal complexes. By examining the molecular orbitals of Figure 9, it is likely that the HOMO will be most affected by the presence of a metal, as this orbital does not have a node at the center. The extent of perturbation of the absorption properties will depend of the eletronegativity of the metal and the conformation it imposes on the macrocycle. As with porphyrins, the emission properties will be governed by the nature of the metal to render complexes fluorescent, phosphorescent, or nonemissive. The DFT calculations of this study indicate that the LUMO and HOMO−1 are most affected by bromination, and hence serial bromination of a metallocorrole should lead to a red shift of all spectral features and an increase in the oscillator strength of the lowest-energy absorption features, as observed for the free-base corroles in this study. The precise extent of the perturbation of bromination on the metallocorroles is under investigation.

## CONCLUSIONS

The combined experimental and computational examination of compounds **2**–**6** has provided insight into the basic photophysics of free-base $\beta$-substituted corroles. Serial bromination of the corrole periphery at the $\beta$ positions greatly perturbs the four frontier molecular orbital manifold of $N_4$ macrocycles. TD-DFT calculations corroborate spectral assignments, which are governed by two Q states and two B (Soret) states with orthogonal polarization. The Soret band splits upon increasing bromination as a result of the asymmetry along the $x$- and $y$-axes of the corrole core. This study has helped to contextualize previous observations of a split Soret band. We contend that there are always two Soret transitions, as dictated by the symmetry of the corrole framework. The ability to resolve the bands depends on the electronic nature of the substituents and the polarity of the solvent in which the spectrum is obtained.

In addition to the red shift of observed spectral features, the inclusion of bromine atoms produces a pronounced heavy atom effect, which is the primary determinant of the photophysical properties of the free-base corrole. Bromination decreases the fluorescence quantum yield and lifetime by promoting


DOI: 10.1021/ic502860g
Inorg. Chem. 2015, 54, 2713–2725

enhanced intersystem crossing, as evidenced by a dramatic increase in $k_{nr}$ with bromine substitution. A nonbrominated dimer exhibits absorption and emission features comparable to the tetrabrominated derivative, suggesting that oligomerization is a means of red-shifting the spectral properties akin to bromination but without decreasing the fluorescence quantum yield. With this understanding of the photophysical properties of free-base corroles, we are currently exploring applications of these platforms as energy-transfer acceptors within quantum dot−corrole conjugates for optical chemosensing applications.

## ■ ASSOCIATED CONTENT

### Supporting Information

Synthetic procedures for the synthesis of compound **1** in addition to $^{1}H$ and $^{19}F$ NMR spectra for all compounds. Summaries of crystallographic data, TA spectral data, and results of DFT calculations (including optimized geometries, molecular orbital illustrations, simulated UV−vis spectra, tables of Cartesian coordinates, and tables of TD-DFT results). This material is available free of charge via the Internet at http://pubs.acs.org.

## ■ AUTHOR INFORMATION


### Corresponding Author

*E-mail: dnocera@fas.harvard.edu.



### Funding

This material is based upon work supported by the U.S. Department of Energy Office of Science, Office of Basic Energy Sciences under Award No. DE-SC0009758.


### Notes

The authors declare no competing financial interest.

## ■ ACKNOWLEDGMENTS


C.M.L. acknowledges the National Science Foundation's Graduate Research Fellowship Program. We thank Bryce Anderson and Andrew Maher for assistance with experiments using the Libra-F-HE laser system as well as Casandra Cox and Bon Jun . Koo for the images used in the TOC graphic. Calculations were performed using the Odyssey cluster supported by FAS Research Computing.


## ■ REFERENCES


(1) Mody, T. D.; Sessler, J. L. In *Perspectives Supramolecular Chemistry;* Reinhoudt, D. N., Ed.; John Wiley & Sons: Chichester, U.K., 1999; pp 245−294.
(2) Vicente, M. G. H. *Curr. Med. Chem. Anti-Cancer Agents* **2001**, *1*, 175−194.
(3) Berg, K.; Selbo, P. K.; Weyergang, A.; Dietze, A.; Prasmickaite, L.; Bonsted, A.; Engesaeter, B. Ø.; Angell-Petersen, E.; Warloe, T.; Frandsen, N.; Høgset, A. *J. Microsc.* **2005**, *218*, 133−147.
(4) Ethirajan, M.; Chen, Y.; Joshi, P.; Pandey, R. K. *Chem. Soc. Rev.* **2011**, *40*, 340−362.
(5) Bonnett, R. *Chem. Soc. Rev.* **1995**, 19−33.
(6) Sternberg, E. D.; Dolphin, D.; Brückner, C. *Tetrahedron* **1998**, *54*, 4151−4202.
(7) O'Connor, A. E.; Gallagher, W. M.; Byrne, A. T. *Photochem. Photobiol.* **2009**, *85*, 1053−1074.
(8) Kim, D.; Osuka, A. *Acc. Chem. Res.* **2004**, *37*, 735−745.
(9) Imahori, H. *J. Phys. Chem. B* **2004**, *108*, 6130−6143.
(10) Imahori, H.; Umeyama, T.; Ito, S. *Acc. Chem. Res.* **2009**, *42*, 1809−1818.
(11) Martínez-Díaz, M. V.; de la Torre, G.; Torres, T. *Chem. Commun.* **2010**, *46*, 7090−7108.
(12) Papkovsky, D. B. *Sens. Actuators, B* **1993**, *11*, 293−300.
(13) Papkovsky, D. B.; Ponomarev, G. V.; Trettnak, W.; O'Leary, P. *Anal. Chem.* **1995**, *67*, 4112−4117.
(14) Papkovsky, D. B.; O'Riordan, T.; Soini, A. *Biochem. Soc. Trans.* **2000**, *28*, 74−77.
(15) Zhang, X. B.; Guo, C. C.; Li, Z. Z.; Shen, G. L.; Yu, R. Q. *Anal. Chem.* **2002**, *74*, 821−825.
(16) Johnson, A. W.; Kay, I. T. *Proc. Chem. Soc.* **1964**, 89−90.
(17) Johnson, A. W.; Kay, I. T. *J. Chem. Soc.* **1965**, 1620−1629.
(18) Gross, Z.; Galili, N.; Saltsman, I. *Angew. Chem., Int. Ed.* **1999**, *38*, 1427−1429.
(19) Gross, Z.; Galili, N.; Simkhovich, L.; Saltsman, I.; Botoshansky, M.; Bläser, D.; Boese, R.; Goldberg, I. *Org. Lett.* **1999**, *1*, 599−602.
(20) Paolesse, R.; Jaquinod, L.; Nurco, D. J.; Mini, S.; Sagone, F.; Boschi, T.; Smith, K. M. *Chem. Commun.* **1999**, 1307−1308.
(21) Paolesse, R.; Nardis, S.; Sagone, F.; Khoury, R. G. *J. Org. Chem.* **2001**, *66*, 550−556.
(22) Paolesse, R. In *The Porphyrin Handbook;* Kadish, K. M., Smith, K. M., Guilard, R., Eds.; Academic Press: San Diego, CA, 2000; Vol. *2*; pp 201−232.
(23) Nardis, S.; Monti, D.; Paolesse, R. *Mini-Rev. Org. Chem.* **2005**, *2*, 355−374.
(24) Paolesse, R. *Synlett* **2008**, 2215−2230.
(25) Gryko, D. T. *J. Porphyrins Phthalocyanines* **2008**, *12*, 906−917.
(26) Lemon, C. M.; Brothers, P. J. *J. Porphyrins Phthalocyanines* **2011**, *15*, 809−834.
(27) Barata, J. F. B.; Santos, C. I. M.; Neves, M. G. P. M. S.; Faustino, M. A. F.; Cavaleiro, J. A. S. *Top. Heterocycl. Chem.* **2014**, *33*, 79−142.
(28) Aviv, I.; Gross, Z. *Chem. Commun.* **2007**, 1987−1999.
(29) Aviv-Harel, I.; Gross, Z. *Chem.—Eur. J.* **2009**, *15*, 8382−8394.
(30) Aviv-Harel, I.; Gross, Z. *Coord. Chem. Rev.* **2011**, *255*, 717−736.
(31) Gross, Z.; Golubkov, G.; Simkhovich, L. *Angew. Chem., Int. Ed.* **2000**, *39*, 4045−4047.
(32) Mahammed, A.; Gray, H. B.; Meier-Callahan, A. E.; Gross, Z. *J. Am. Chem. Soc.* **2003**, *125*, 1162−1163.
(33) Gross, Z.; Gray, H. B. *Adv. Synth. Catal.* **2004**, *364*, 165−170.
(34) Dogutan, D. K.; Stoian, S. A.; McGuire, R.; Schwalbe, M.; Teets, T. S.; Nocera, D. G. *J. Am. Chem. Soc.* **2011**, *133*, 131−140.
(35) Dogutan, D. K.; McGuire, R.; Nocera, D. G. *J. Am. Chem. Soc.* **2011**, *133*, 9178−9180.
(36) Lemon, C. M.; Dogutan, D. K.; Nocera, D. G. In *Handbook of Porphyrin Science;* Kadish, K. M., Smith, K. M., Guilard, R., Eds.; World Scientific Publishing: Singapore, 2012; Vol. *21*; pp 1−143.
(37) Luobeznova, I.; Raizman, M.; Goldberg, I.; Gross, Z. *Inorg. Chem.* **2006**, *45*, 386−394.
(38) Wagnert, L.; Berg, A.; Stavitski, E.; Luobeznova, I.; Gross, Z.; Levanon, H. *J. Porphyrins Phthalocyanines* **2007**, *11*, 645−651.
(39) Agadjanian, H.; Ma, J.; Rentsendorj, A.; Valluripalli, V.; Hwang, J. Y.; Mahammed, A.; Farkas, D. L.; Gray, H. B.; Gross, Z.; Medina-Kauwe, L. K. *Proc. Natl. Acad. Sci. U.S.A.* **2009**, *106*, 6105−6110.
(40) Ventura, B.; Esposti, A. D.; Koszarna, B.; Gryko, D. T.; Flamigni, L. *New J. Chem.* **2005**, *29*, 1559−1566.
(41) Shao, W.; Wang, H.; He, S.; Shi, L.; Peng, K.; Lin, Y.; Zhang, L.; Ji, L.; Liu, H. *J. Phys. Chem. B* **2012**, *116*, 14228−14234.
(42) Hwang, J. Y.; Gross, Z.; Gray, H. B.; Medina-Kauwe, L. K.; Farkas, D. L. *J. Biomed. Opt.* **2011**, *16*, 066007/1−6.
(43) Ding, T.; Alemán, E. A.; Modarelli, D. A.; Ziegler, C. J. *J. Phys. Chem. A* **2005**, *109*, 7411−7417.
(44) Shi, L.; Liu, H. Y.; Shen, H.; Hu, J.; Zhang, G. L.; Wang, H.; Ji, L. N.; Chang, C. K.; Jiang, H. F. *J. Porphyrins Phthalocyanines* **2009**, *13*, 1221−1226.
(45) Zhan, H. Y.; Liu, H. Y.; Lu, J.; Wang, A. Z.; You, L. L.; Wang, H.; Ji, L. N.; Jiang, H. F. *J. Porphyrins Phthalocyanines* **2010**, *14*, 150−157.
(46) Ngo, T. H.; Puntoriero, F.; Nastasi, F.; Robeyns, K.; Van Meervelt, L.; Campagna, S.; Dehaen, W.; Maes, W. *Chem.—Eur. J.* **2010**, *16*, 5691−5705.
(47) Ivanova, Y. B.; Savva, V. A.; Mamardashvili, N. Z.; Starukhin, A. S.; Ngo, T. H.; Dehaen, W.; Maes, W.; Kruk, M. M. *J. Phys. Chem. A* **2012**, *116*, 10683−10694.




DOI: 10.1021/ic502860g
*Inorg. Chem.* 2015, 54, 2713−2725

(48) Kruk, M.; Ngo, T. H.; Verstappen, P.; Starukhin, A.; Hofkens, J.; Dehaen, W.; Maes, W. *J. Phys. Chem. A* **2012**, *116*, 10695−10703.
(49) Kruk, M.; Ngo, T. H.; Savva, V.; Starukhin, A.; Dehaen, W.; Maes, W. *J. Phys. Chem. A* **2012**, *116*, 10704−10711.
(50) Beenken, W.; Pressely, M.; Ngo, T. H.; Dehaen, W.; Maes, W.; Kruk, M. *J. Phys. Chem. A* **2014**, *118*, 862−871.
(51) Flamigni, L.; Ventura, B.; Tasior, M.; Gryko, D. T. *Inorg. Chim. Acta* **2007**, *360*, 803−813.
(52) Tasior, M.; Gryko, D. T.; Cembor, M.; Jaworski, J. S.; Ventura, V.; Flamigni, L. *New J. Chem.* **2007**, *31*, 247−259.
(53) Tasior, M.; Gryko, D. T.; Pielacinska, D. J.; Zanelli, A.; Flamigni, L. *Chem.—Asian J.* **2010**, *5*, 130−140.
(54) Vestfrid, J.; Goldberg, I.; Gross, Z. *Inorg. Chem.* **2014**, *53*, 10536−10542.
(55) Laha, J. K.; Dhanalekshmi, S.; Taniguchi, M.; Ambroise, A.; Lindsey, J. S. *Org. Process Res. Dev.* **2003**, *7*, 799−812.
(56) Zaidi, S. H. H.; Loewe, R. S.; Clark, B. A.; Jacob, M. J.; Lindsey, J. S. *Org. Process Res. Dev.* **2006**, *10*, 304−314.
(57) Lemon, C. M. M.S. Thesis, Massachusetts Institute of Technology: Cambridge, MA, U.S.A., 2013.
(58) Fulmer, G. R.; Miller, A. J. M.; Sherden, N. H.; Gottlieb, H. E.; Nudelman, A.; Stoltz, B. M.; Bercaw, J. E.; Goldberg, K. I. *Organometallics* **2010**, *29*, 2176−2179.
(59) *CRC Handbook of Chemistry and Physics,* 73rd ed.; CRC Press: Boca Raton, FL, 1992.
(60) Seybold, P. G.; Gouterman, M. *J. Mol. Spectrosc.* **1969**, *31*, 1−13.
(61) Lemon, C. M.; Karnas, E.; Bawendi, M. G.; Nocera, D. G. *Inorg. Chem.* **2013**, *52*, 10394−10406.
(62) Loh, Z. H.; Miller, S. E.; Chang, C. J.; Carpenter, S. D.; Nocera, D. G. *J. Phys. Chem. A* **2002**, *106*, 11700−11708.
(63) Pizano, A. A.; Lutterman, D. A.; Holder, P. G.; Teets, T. S.; Stubbe, J.; Nocera, D. G. *Proc. Natl. Acad. Sci. U.S.A.* **2012**, *109*, 39−43.
(64) Holder, P. G.; Pizano, A. A.; Anderson, B. L.; Stubbe, J.; Nocera, D. G. *J. Am. Chem. Soc.* **2012**, *134*, 1172−1180.
(65) Becke, A. D. *Phys. Rev. A* **1988**, *38*, 3098−3100.
(66) Becke, A. D. *J. Chem. Phys.* **1993**, *98*, 1372−1377.
(67) Becke, A. D. *J. Chem. Phys.* **1993**, *98*, 5648−5652.
(68) Lee, C.; Yang, W.; Parr, R. G. *Phys. Rev. B* **1988**, *37*, 785−789.
(69) Frisch, M. J.; et al. *Gaussian 09,* Revision D.01; Gaussian, Inc.: Wallingford, CT, 2009.
(70) Wadt, W. R.; Hay, P. J. *J. Chem. Phys.* **1985**, *82*, 284−298.
(71) Hay, P. J.; Wadt, W. R. *J. Chem. Phys.* **1985**, *82*, 299−310.
(72) Barone, V.; Cossi, M. *J. Phys. Chem. A* **1998**, *102*, 1995−2001.
(73) Cossi, M.; Rega, N.; Scalmani, G.; Barone, V. *J. Comput. Chem.* **2003**, *24*, 669−681.
(74) Bauernschmitt, R.; Ahlrichs, R. *Chem. Phys. Lett.* **1996**, *256*, 454−464.
(75) Casida, M. E.; Jamorski, C.; Casida, K. C.; Salahub, D. R. *J. Chem. Phys.* **1998**, *108*, 4439−4449.
(76) Stratmann, R. E.; Scuseria, G. E.; Frisch, M. J. *J. Chem. Phys.* **1998**, *109*, 8218−8224.
(77) Van Caillie, C.; Amos, R. D. *Chem. Phys. Lett.* **1999**, *308*, 249−255.
(78) Scalmani, G.; Frisch, M. J.; Mennucci, B.; Tomasi, J.; Cammi, R.; Barone, V. *J. Chem. Phys.* **2006**, *124*, 094107/1−15.
(79) Hanwell, M. D.; Curtis, D. E.; Lonie, D. C.; Vandermeersch, T.; Zurek, E.; Hutchison, G. R. *J. Cheminf.* **2012**, *4*, 17/1−17.
(80) Sheldrick, G. M. *Acta Crystallogr., Sect. A: Found. Crystallogr.* **2008**, *A64*, 112−122.
(81) Golubkov, G.; Bendix, J.; Gray, H. B.; Mahammed, A.; Goldberg, I.; DiBilio, A. J.; Gross, Z. *Angew. Chem., Int. Ed.* **2001**, *40*, 2132−2134.
(82) Wasbotten, I. H.; Wondimagegn, T.; Ghosh, A. *J. Am. Chem. Soc.* **2002**, *124*, 8104−8116.
(83) Palmer, J. H.; Day, M. W.; Wilson, A. D.; Henling, L. M.; Gross, Z.; Gray, H. B. *J. Am. Chem. Soc.* **2008**, *130*, 7786−7787.
(84) Nardis, S.; Mandoj, F.; Paolesse, R.; Fronczek, F. R.; Smith, K. M.; Prodi, L.; Montalti, M.; Battistini, G. *Eur. J. Inorg. Chem.* **2007**, 2345−2352.
(85) Du, R. B.; Liu, C.; Shen, D. M.; Chen, Q. Y. *Synlett* **2009**, 2701−2705.
(86) Tortora, L.; Nardis, S.; Fronczek, F. R.; Smith, K. M.; Paolesse, R. *Chem. Commun.* **2011**, *47*, 4243−4245.
(87) Scrivanti, A.; Beghetto, V.; Matteoli, U.; Antonaroli, S.; Marini, A.; Mandoj, F.; Paolesse, R.; Crociani, B. *Tetrahedron Lett.* **2004**, *45*, 5861−5864.
(88) Koszarna, B.; Gryko, D. T. *J. Org. Chem.* **2006**, *71*, 3707−3717.
(89) Barata, J. F. B.; Silva, A. M. G.; Neves, M. G. P. M. S.; Tomé, A. C.; Silva, A. M. S.; Cavaleiro, J. A. S. *Tetrahedron Lett.* **2006**, *47*, 8171−8174.
(90) Hiroto, S.; Furukawa, K.; Shinokubo, H.; Osuka, A. *J. Am. Chem. Soc.* **2006**, *128*, 12380−12381.
(91) Hirabayshi, S.; Omote, M.; Aratani, N.; Osuka, A. *Bull. Chem. Soc. Jpn.* **2012**, *85*, 558−562.
(92) Ding, T.; Harvey, J. D.; Ziegler, C. J. *J. Porphyrins Phthalocyanines* **2005**, *9*, 22−27.
(93) Reith, L. M.; Stiftinger, M.; Monkowius, U.; Knör, G.; Schoefberger, W. *Inorg. Chem.* **2011**, *50*, 6788−6797.
(94) Gouterman, M. In *The Porphyrins;* Dolphin, D., Ed.; Academic Press: New York, 1978; Vol. 3; pp 1−165.
(95) Dreuw, Z.; Head-Gordon, M. *Chem. Rev.* **2005**, *105*, 4009−4037.
(96) Jacquemin, D.; Wathelet, V.; Perpète, E. A.; Adamo, C. *J. Chem. Theory Comput.* **2009**, *5*, 2420−2435.
(97) Jacquemin, D.; Mennucci, B.; Adamo, C. *Phys. Chem. Chem. Phys.* **2011**, *13*, 16987−16998.
(98) Gross, Z.; Gray, H. B. *Comments Inorg. Chem.* **2006**, *27*, 61−72.
(99) Geier, G. R.; Chick, J. F. B.; Callinan, J. B.; Reid, C. G.; Auguscinski, W. P. *J. Org. Chem.* **2004**, *69*, 4159−4169.
(100) Gouterman, M. *J. Chem. Phys.* **1959**, *30*, 1139−1161.
(101) Gouterman, M. *J. Mol. Spectrosc.* **1961**, *6*, 138−163.
(102) Gouterman, M.; Wagnière, G. H.; Snyder, L. C. *J. Mol. Spectrosc.* **1963**, *11*, 108−127.
(103) Ghosh, A.; Wondimagegn, T.; Parusel, A. B. J. *J. Am. Chem. Soc.* **2000**, *122*, 5100−5104.
(104) Albrett, A. M.; Conradie, J.; Ghosh, A.; Brothers, P. J. *Dalton Trans.* **2008**, 4464−4473.
(105) Bendix, J.; Dmochowski, I. J.; Gray, H. B.; Mahammed, A.; Simkhovich, L.; Gross, Z. *Angew. Chem., Int. Ed.* **2000**, *39*, 4048−4051.
(106) Simkhovich, L.; Goldberg, I.; Gross, Z. *J. Inorg. Biochem.* **2000**, *80*, 235−238.
(107) Ziegler, C. J.; Sabin, J. R.; Geier, G. R.; Nemykin, V. N. *Chem. Commun.* **2012**, *48*, 4743−4745.
(108) Ripin, D. H.; Evans, D. A. *Evans p$K_a$ Table.* http://evans.harvard.edu/pdf/evans_pka_table.pdf.
(109) Balazs, Y. S.; Saltsman, I.; Mahammed, A.; Tkachenko, E.; Golubkov, G.; Levine, J.; Gross, Z. *Magn. Reson. Chem.* **2004**, *42*, 624−635.
(110) Koszarna, B.; Gryko, D. T. *Chem. Commun.* **2007**, 2994−2996.
(111) Gryko, D. T.; Jadach, K. *J. Org. Chem.* **2001**, *66*, 4267−4275.
(112) Egorova, O. A.; Tsay, O. G.; Khatua, S.; Meka, B.; Maiti, N.; Kim, M. K.; Kwon, S. J.; Huh, J. O.; Bucella, D.; Kang, S. O.; Kwak, J.; Churchill, D. G. *Inorg. Chem.* **2010**, *49*, 502−512.
(113) Gryko, D. T.; Koszarna, B. *Synthesis* **2004**, 2205−2209.
(114) Rohrdanz, M. A.; Herbert, J. M. *J. Chem. Phys.* **2008**, *129*, 034107/1−9.
(115) Siebrand, W. *J. Chem. Phys.* **1967**, *46*, 440−447.
(116) Siebrand, W. *J. Chem. Phys.* **1967**, *47*, 2411−2422.


DOI: 10.1021/ic502860g
*Inorg. Chem.* 2015, 54, 2713−2725